

Influence of pH on Structural, Morphological, Optical, Photocatalytic, and Antibacterial Properties of Yttrium Oxide Nanoparticles via Co-Precipitation Method

Kiruthika Parangusan

PSG College of Arts and Science

Venkat Subramaniam (✉ venkatnanotechnology@gmail.com)

PSG College of Arts and Science

Lakshmanaperumal Sundarabharathi

S.S. Duraisamy Nadar Mariammal College

Karthik Kannan

Kumoh National Institute of Technology

Devi Radhika

Jain-Deemed to be University

Research Article

Keywords: Yttrium oxide, co-precipitation method, MB dye, foodborne pathogens

Posted Date: April 8th, 2021

DOI: <https://doi.org/10.21203/rs.3.rs-385905/v1>

License: © ⓘ This work is licensed under a Creative Commons Attribution 4.0 International License.

[Read Full License](#)

Influence of pH on structural, morphological, optical, photocatalytic, and antibacterial properties of yttrium oxide nanoparticles via co-precipitation method

**Kiruthika Parangusan¹, Venkat Subramaniam^{1*}, Lakshmanaperumal Sundarabharathi²,
Karthik Kannan³, Devi Radhika⁴**

¹*Department of Electronics, PSG college of Arts and Science, Coimbatore, Tamil Nadu, India*

²*Department of Physics, S.S. Duraisamy Nadar Mariammal College, Kovilpatti, Tamil Nadu, India.*

³*School of Advanced Materials Science and Engineering, Kumoh National Institute of Technology, 61 Daehak-ro, Gumi-si, Gyeongbuk 39177, Republic of Korea*

⁴*Department of Chemistry, School of Engineering and Technology, Jain-Deemed to be University, Jakkasandra, Ramnagara-562112, Karnataka, India.*

*Corresponding author: venkatnanotechnology@gmail.com

Abstract

Yttrium oxide nanoparticles with multiform morphologies have been synthesized by the co-precipitation method. The structure, morphology, functional groups, optical and photoluminescence properties were examined through X-ray diffraction (XRD), Scanning electron microscope (SEM), Fourier transform infrared spectrometer (FTIR), UV-Visible (UV-Vis), Photoluminescence spectra (PL). The XRD patterns obtained for the samples synthesized at various pH values confirmed the cubic structure of Y₂O₃. The patterns obtained on the samples at pH values of 8 and 9 appeared as have sharp peaks suggested, that the samples were well crystallized. From UV-vis spectra, it revealed that the bandgap energy exhibits a blue shift in the absorption edge for the samples with the increase of pH due to their changing morphologies and surface structures. In the PL spectra, the obtained Y₂O₃ samples demonstrate an intense and bright UV and blue emission under the excitation wavelength range of 250 nm. The photocatalytic degradation of the Y₂O₃ nanostructure was studied against the Methylene blue (MB) dye under sunlight irradiation. The results showed good recital under solar light irradiation. Further, the antimicrobial activities of Y₂O₃ nanostructure against foodborne pathogens (*Staphylococcus aureus* and *Salmonella typhi*) were examined by using the disc diffusion method. Moreover, the Y₂O₃ nanostructure was found to be biocompatible.

Keywords: Yttrium oxide; co-precipitation method; MB dye; foodborne pathogens.

1. Introduction

Currently, tremendous efforts have been focused on the studies of modern nanomaterials and their impending applications. With increasing industrial demands, it exhibits a smaller size, well crystalline nature, and better nanostructures adopted for electronic devices and wastewater remediation applications. Rare earth metal oxide nanoparticles are extensively studied in the field of nanomaterials due to their peculiar nanostructures, optical, electronic, and catalytic properties [1]. All these features are favorable to several technological applications like as optical communication, optical display device, photocatalytic, medical diagnosis, and UV shielding [1-7]. In addition, Fluorescent based nanomaterials versatile role in the area of UV and visible light emission devices [8, 9]. The compounds based on rare earth metals have been widely utilized as high recital luminescent materials, because of their properties within the nano-scale range might be related to their morphology [10, 11]. Among all rare-earth oxides, yttrium oxide (Y_2O_3) nanoparticles have also been significantly reviewed as a host material that used upconversion efficiency because of their extensive range of optical transparency large bandgap (5.8 eV) and other optical and biological applications [12,13].

The morphology and structure of materials chiefly depend upon the fabrication circumstances and limitations [14]. So far, numerous techniques employed for the fabrication of Y_2O_3 nanostructures, such as sol-gel [15], hydrothermal [16], and combustion synthesis [17]. Amid these, the co-precipitation route extends renowned benefits counting sample purity, low cost, and eases to production. In this method, the preparation of particles is below hundred nanometers, easily control the particle size by changing the hydrolysis time and regulate the shape of the particles by changing the pH value of the aqueous solution [18]. This size control and shape are desirable to generate well optoelectronic material. Hence, in this work synthesize Y_2O_3 nanoparticles with well-ordered particle size and shape by the trouble-free alteration of the pH value of the solution. The manipulate of pH on the purity, crystallinity, morphology, optical, and emission properties has been investigated through XRD, FTIR, SEM, UV-Vis, photoluminescence, photocatalytic and biological studies.

2. Experimental

2.1. Synthesis of yttrium oxide nanoparticles

Yttrium oxide nanoparticles were synthesized by the co-precipitation route. The initial chemicals consumed in this process were of analytical grade without any supplementary cleansing. The yttrium nitrate hexahydrate ($\text{Y}(\text{NO})_3 \cdot 6\text{H}_2\text{O}$) was used as a forerunner material and ammonium hydroxide employed as a precipitating agent (varying pH values). Then, the precise amount of yttrium nitrate was suspended in 50 mL of deionized water (DD) and stirred well through a magnetic stirrer. The pH (7, 8, and 9) readings of the solution were separately regulated by ammonium hydroxide; the above were combined through steady stirring for 2 h at 353 K. Finally, the white precipitate was obtained. The accomplished precipitate was filtered off and cleaned a several times with DD and ethanol. The resultant white gel was dehydrated at 353 K for approximately 3 h in a hot air oven and next calcinated at 773 K for 2 h.

2.2. Characterization techniques

The phase of the fabricated samples were examined by XRD operating the PANalytical model X'PERT-PRO spectrometer K_α radiations ($\lambda = 1.5418 \text{ \AA}$). FTIR spectra were recorded using the Shimadzu model 8400S spectrometer (4000 cm^{-1} to 400 cm^{-1}). For this analysis, a small amount of Y_2O_3 samples was blended with KBr and then pressed into pellets for the measurement. The changes in surface morphology of the products were observed by (SEM, S-4200, Hitachi) functioned at 15 kV. The UV-vis absorption spectra were obtained on the Agilent 8453 diode array UV-Vis spectrophotometer. Photoluminescence was examined on a Cary eclipse spectrophotometer with a UV light as the excitation light source.

The photocatalytic action of the Y_2O_3 (pH=9) was appraised by handling a strategy interpreted in [35] although the antibacterial action of the Y_2O_3 (pH=9) was explored by agar well diffusion method portrayed elsewhere [35].

3. Results and Discussions

3.1. Structural analysis

The XRD peaks of yttrium oxide nanoparticles with various pH values that were different from 7 to 9 are revealed in Fig. 1. The peaks at 2θ values of 20.49° , 29.119° , 33.75° , 39.25° , 43° ,

48.46°, and 57.56° relate to the (211), (222), (400), (332), (134), (440) and (622) crystal planes and it verifies the cubic structure of Y₂O₃. The obtained peaks of all fitted with the customary JCPDS card [89-5591]. No secondary peaks (unwanted impurities) are noticed in the XRD, which designates that are highly phase pure compounds. At the optimum value of pH, supersaturation becomes the highest value and the radius of crystallites will be formed as a lowest, which is due to the circumstance that larger concentration of solute (supersaturation) guides to the initiation of a huge numeral of nucleation sites and more nuclei means smaller sized nuclei. For pH values 8 and 9 of the samples, more sharp peaks obtained which suggested that the synthesized samples were highly crystallized. Though, the Y₂O₃ nanoparticles achieved from the solution of pH=7 revealed reasonably less crystallinity and crystallite size. Fig. 1 exhibits a slightly broad peak for pH = 7 and 8 which results from diminished crystallite size contrasted to the higher value of pH = 9 illustrated in Table 1.

The average crystallite size (Debye-Scherrer) of yttrium oxide nanoparticles was attained by this equation 1 [19]

$$D = \frac{0.9\lambda}{\beta \cos\theta} \quad (1)$$

Where ‘β’ signifies the full width at half maximum (FWHM) of XRD peaks, ‘θ’ is the Bragg’s angle of diffraction lines, ‘λ’ is an incident wavelength of X- rays. The crystallite size is measured from the XRD and it is found to be 13 - 16 nm which was displayed in Table 1. For cubic structure, the Lattice constant (a) is obtained from d_{hkl} as given below

$$\frac{1}{d^2} = \frac{h^2 + k^2 + l^2}{a^2} \quad (2)$$

Where ‘d’ is the Inter planar spacing, (h k l) is the Miller indices and ‘a’ is Lattice constant. The calculated lattice value is 10.6020 Å and it is in fine conformity with the customary JCPDS card no- 89-5591.

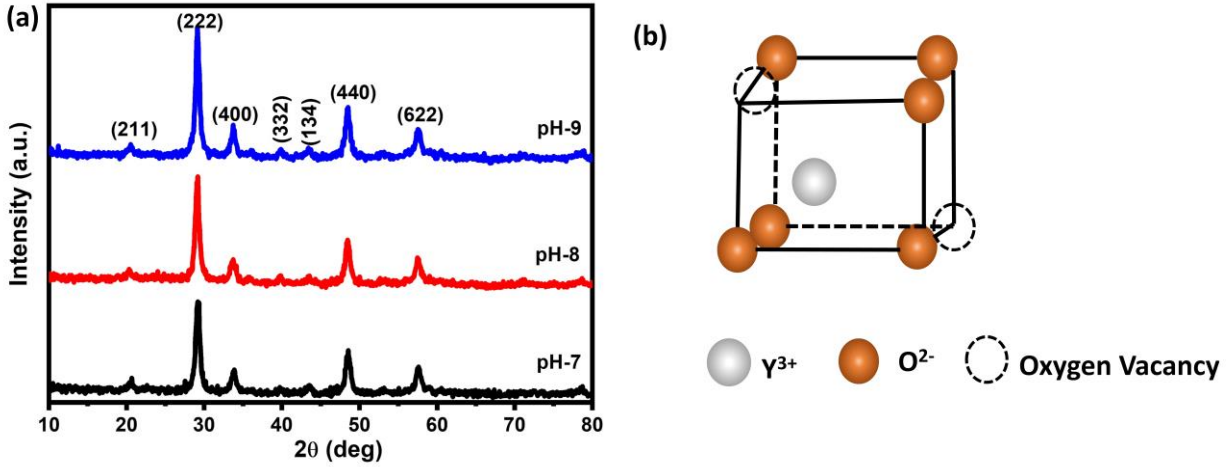


Fig.1. XRD patterns of Y_2O_3 nanoparticles prepared with different pH values

The surface states will take part in a key function in the nanoparticles, because of their huge surface to volume ratio with a lessening in crystallite size [20]. The specific surface area is calculated by using the formula,

$$S = \frac{6 \times 10^8}{D_p \rho} \quad (3)$$

Where ‘S’ is the specific surface area, ‘ D_p ’ is the particle size and ‘ ρ ’ is the density of Y_2O_3 (5.01 g/cm^3). The specific surface area of Y_2O_3 nanoparticles depends on the association amid crystallite size and shape. The dislocation density strongly influences many material properties including strength, size, and defects. The evaluated dislocation density for Y_2O_3 nanoparticles has shown in Table 1.

Table 1

Variation of lattice constants, crystallite size, and energy bandgap of Y_2O_3 nanoparticles synthesized at different pH values.

Samples	Average crystallite size (D) in nm	Lattice parameter (Å) (a=b=c)	SSA (m ² /g) (S)	Dislocation Density x 10 ¹⁵ (lines/m ²) (δ)	Strain (ε)	Bandgap in eV
pH 7	13	10.6020	92.12	8.978	0.0085	3.42
pH 8	14	10.6289	91.12	7.842	0.0035	4.15
pH 9	16	10.6146	74	6.566	0.0016	4.17

3.2. W-H analysis

Williamson-Hall method (W-H) can be applied to compute the microstrain of the fabricated Y₂O₃ nanoparticles. The strain was computed from the horizontal line intercept at the Y-axis, it has a non-zero slope (Fig. 2). From the W-H plot, it is noticed that the strain values are very little and therefore their effect on the broadening of peaks is insignificant [21, 22]. However, there is a minor deviation in the particle size for different pH synthesized samples, due to the presence of strain is account obtained.

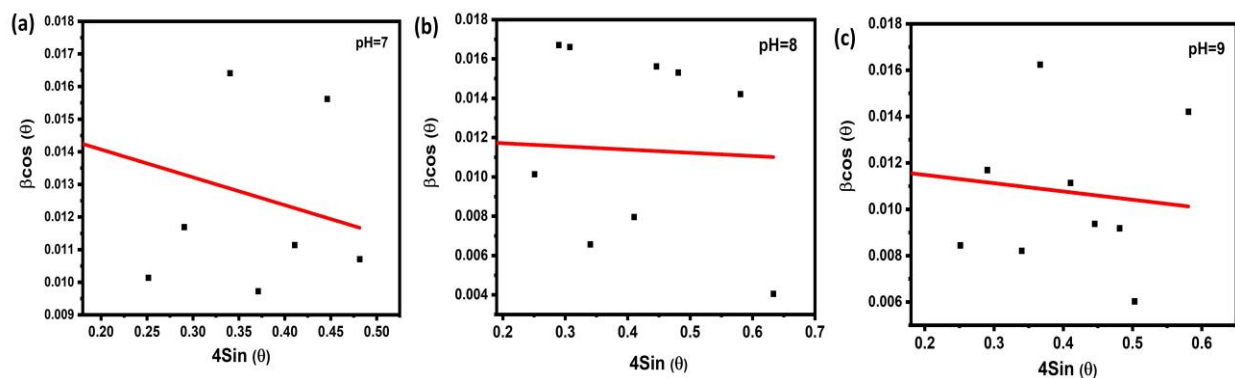


Fig.2. W-H plot for Y₂O₃ nanoparticles synthesized with a different pH value (a) 7 (b) 8 and (c) 9

3.3. Morphological Analysis

SEM micrographs of the fabricated Y_2O_3 nanoparticles with a different pH value are exhibited in Fig. 3 (a-c). The sample synthesized by the solution of pH=7 appeared agglomerated with a spherical nanostructure (Fig. 3a). For pH=8, the Y_2O_3 sample exhibited cube like morphology but it shows a much thinner surface (Fig. 3b). Alternatively, From the SEM image of Y_2O_3 nanoparticles found from the solution of pH=9, the surface morphology different from other samples was detected. The rod-like morphology was observed for the sample synthesized from pH=9 (Fig. 3c). Fig. 3c shows rods like morphology and their average length: 5.75 μm , diameter: 120-450 nm. This designates that pH value is a substantial parameter in adjusting the morphology of Y_2O_3 sample. It is evident from fig. 3 that the increase in pH affected the Yttrium oxide particles owing to the attendance of OH^- ions.

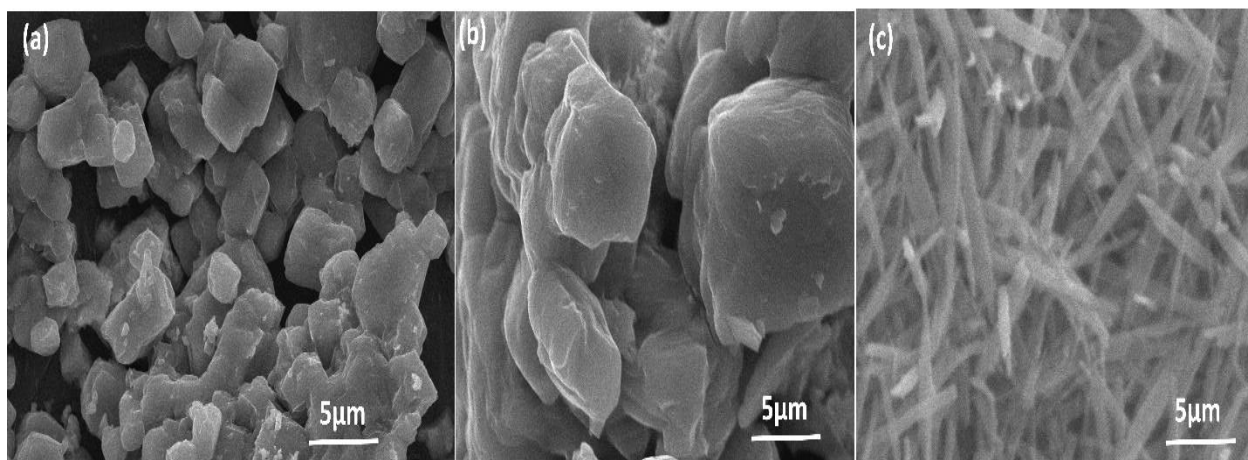


Fig.3. SEM micrographs of Y_2O_3 sample with a diverse pH value (a) pH=7, (b) pH=8 and (c) pH=9

3.4. FTIR studies

The FTIR spectra for the Y_2O_3 samples fabricated with a diverse pH value are depicted in Fig. 4. The peak monitored at 3451 cm^{-1} is because of the stretching vibration of the water molecule [23]. The vibrational peak found at 1633 cm^{-1} was ascribed to the OH vibration. The peak observed at 589 cm^{-1} suggests the stretching vibration of Y-O, which reveals the presence of yttrium oxide in the crystalline phase. It was obvious that the Y-O absorption bands become broader as the particle size diminishes. There were no additional peaks observed in the spectra,

indicating its high phase purity of the sample. Although, the slight change in the wavenumber of the samples fabricated at variant pH values (see Fig.4). This is well matched with the result of the XRD studies.

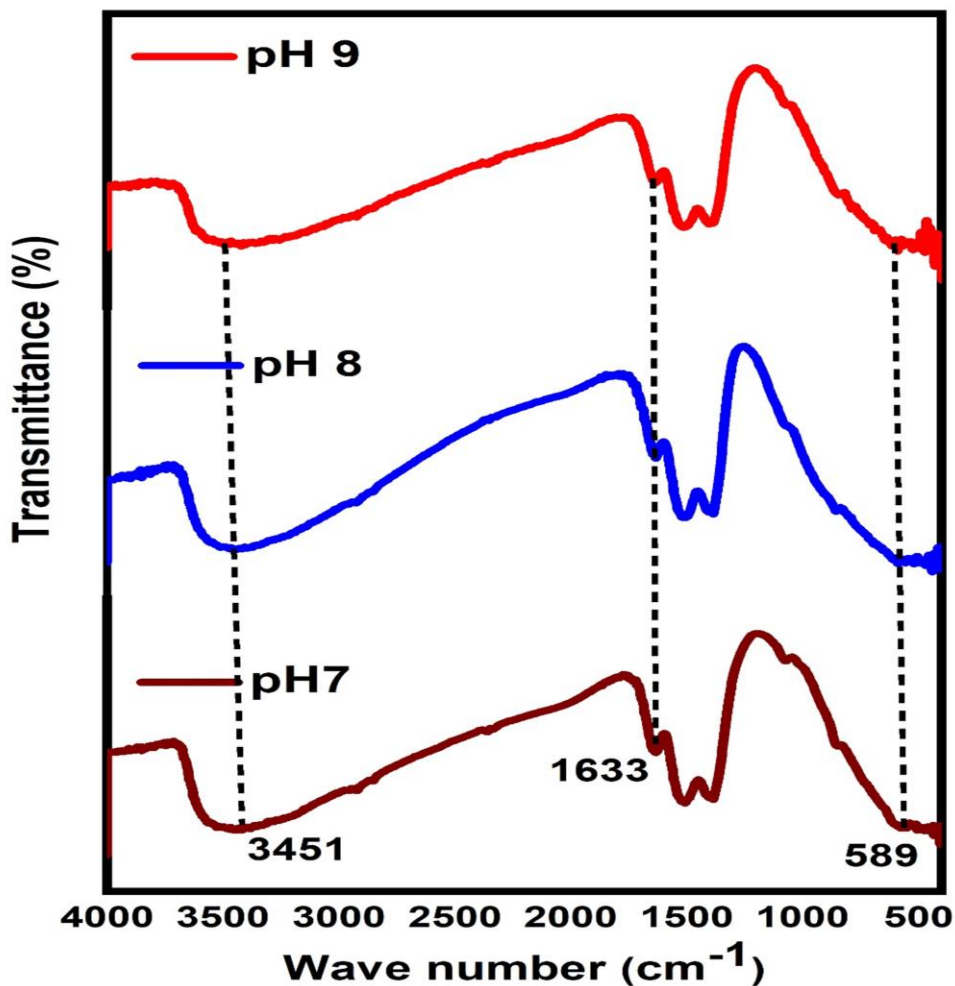


Fig.4. FTIR spectra of Y₂O₃ nanoparticles with a different pH value of 7, 8 and 9

3.5. UV-DRS spectra

The UV-Vis absorbance spectra of Y₂O₃ nanoparticles fabricated with a diverse pH values are displayed in Fig. 5. They exhibit strong absorbance band at around 270 nm; it could be connected to the photoexcitation of electrons from the valance band to conduction band [24].

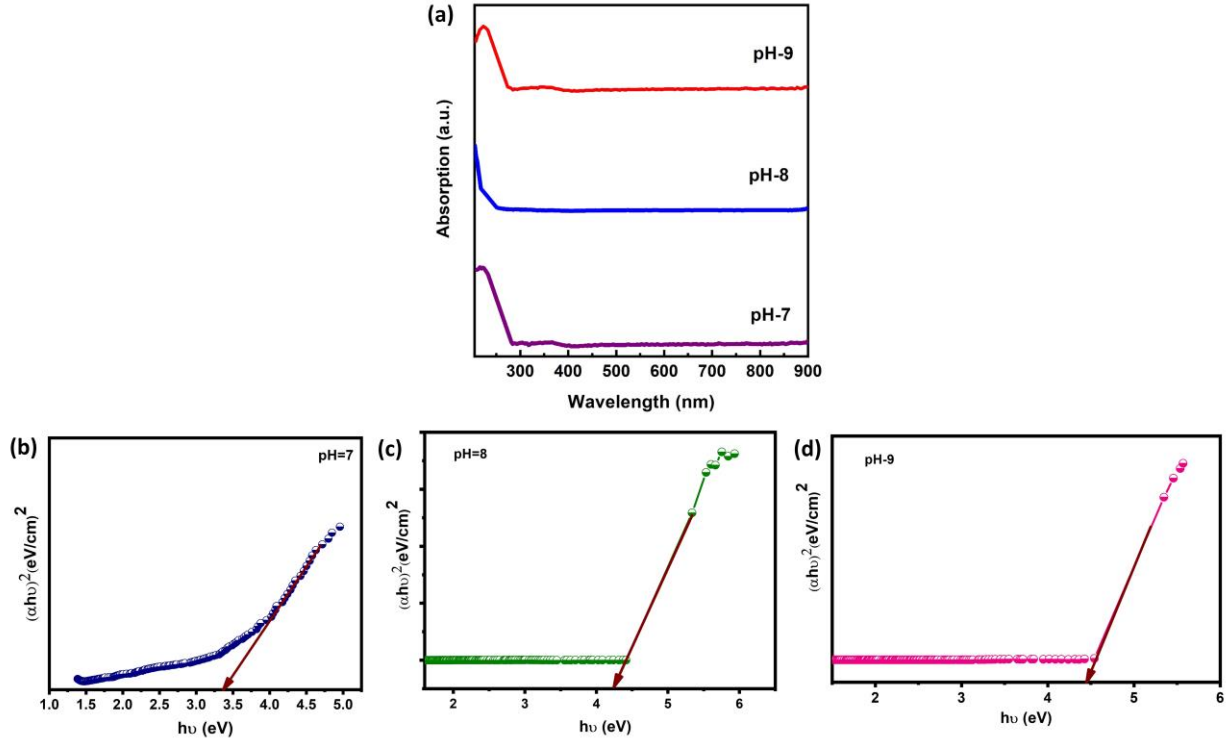


Fig. 5. (a) UV-Vis absorption spectra of Y₂O₃ sample and (b-d) bandgap determination of the Y₂O₃ nanoparticles prepared at different pH 7, 8 and 9

The optical bandgap (E_g) of Y₂O₃ samples was estimated by using Tauc's plot relation. The absorption coefficient is given by equation (4):

$$\alpha(h\nu) = A(h\nu - E_g)^n \quad (4)$$

Where ' $h\nu$ ' is photon energy, ' α ' is absorption coefficient, ' E_g ' is bandgap energy, and ' A ' is the constant related to the material. The exponent $n = 1/2, 2, 3/2,$ and 3 corresponds to the allowed direct and indirect, forbidden direct and forbidden indirect transitions, individually [25, 26]. The bandgap was analyzed from a plot of $(\alpha h\nu)^2$ vs $h\nu$. The bandgap was found to be 3.42, 4.15, 4.47 eV for the Y₂O₃ nanoparticles prepared at pH = 7, 8, and 9 respectively. It has been observed that the bandgap energy reveals a blue move in the absorption edge for the samples with enhancing of pH due to their changing morphologies and surface microstructures [27].

3.6. Photoluminescence analysis

Figure 6 shows the room temperature photoluminescence spectra of Y_2O_3 samples fabricated at various pH values in the emission wavelength range of 270-450 nm. The emission spectra traced under the excitation wavelength range of 250 nm. The Y_2O_3 samples exhibit two emission peaks near band edge (NBE) UV emission and deep level (DL) defects associated with the visible region. The strong UV (NBE) emission at 340-390 nm results from the electron-hole recombination [28, 29]. The Y_2O_3 sample exhibit strong violet emission peak at 420 nm and it is characteristic to the recombination of electrons intensely trapped in oxygen vacancies with photogenerated holes [30]. The intensity of the NBE emission peak depends on the morphology of the product and crystallite size. In this case, the surface morphology of the sample distinct from other samples was observed from SEM, which is in favour of increased intensity in the NBE emission. However, the visible emission is communicated to the oxygen vacancy and interstitial defects within the bandgap of Y_2O_3 nanostructures. The high intensity visible emission shows that the higher pH values needed for high luminescence efficiency. Furthest, this can be accomplished that the pH values play a key function not only in improving the surface morphology of Y_2O_3 nanostructures but also in changing and improving the optical studies of Y_2O_3 nanostructure. The photocatalytic activity of metal oxide nanomaterials surmises the crystallite size, diverse morphologies, and surface defects. In our study, the higher surface defects demonstrated a high impact on the toxic dye degradation.

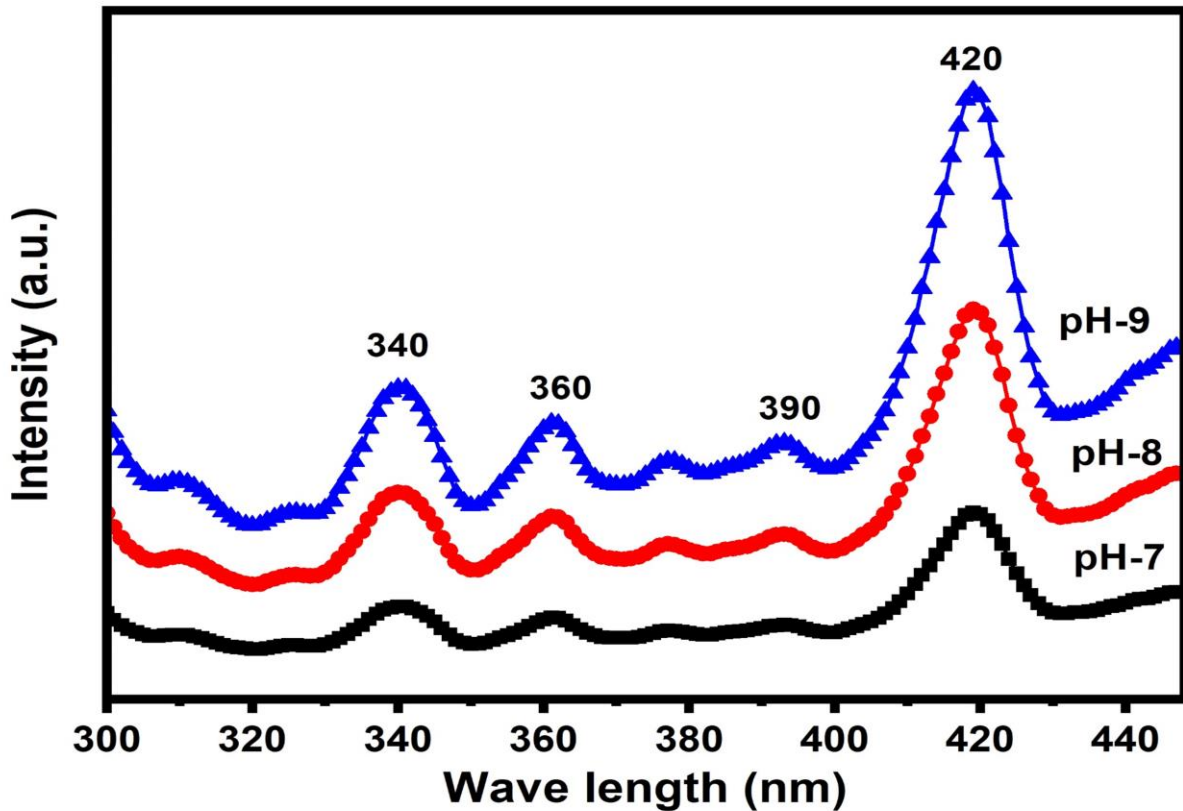


Fig.6. Photoluminescence spectra of Y_2O_3 samples prepared at diverse pH=7, 8 and 9

3.7 Photocatalytic activity

The photocatalytic absorbance spectrum of Y_2O_3 sample (pH=9) beneath sunlight presented in Fig. 7. In the occurrence of Y_2O_3 , the absorbance of the dye (MB) solution decreased with a go up in the irradiation time. From Fig. 8, the characteristic absorption of MB at 662 nm decreased swiftly with the raise in exposure time. This designates that the dye concentration in the solution decreased quickly and virtually vanished in 150 mins. The percentage of degradation was equal to 95 in 150 mins [30-32]. The photocatalytic MB dye degradation follows pseudo-first-order kinetics. It follows from the kinetics study that Y_2O_3 (pH=9) displays a superior photocatalytic activity with a kinetic constant (k) equal to $2.510 \times 10^{-3} \text{ min}^{-1}$.

The recombination of the electron-hole pairs at the surface defect site, and react with the adsorbed O_2 molecule to form superoxide anion $O_2^{\cdot-}$ radical, while the hole reacts with the OH^- surface group to form $\cdot OH$ radicals which can react effectively decompose the dye molecules

into carbon dioxide and water. The main reasons for the enhanced photocatalysis of Y_2O_3 (pH=9) is due to the partition of charge carriers, the reduction of the bandgap, and the rod-like (1-D) structure [33, 34].

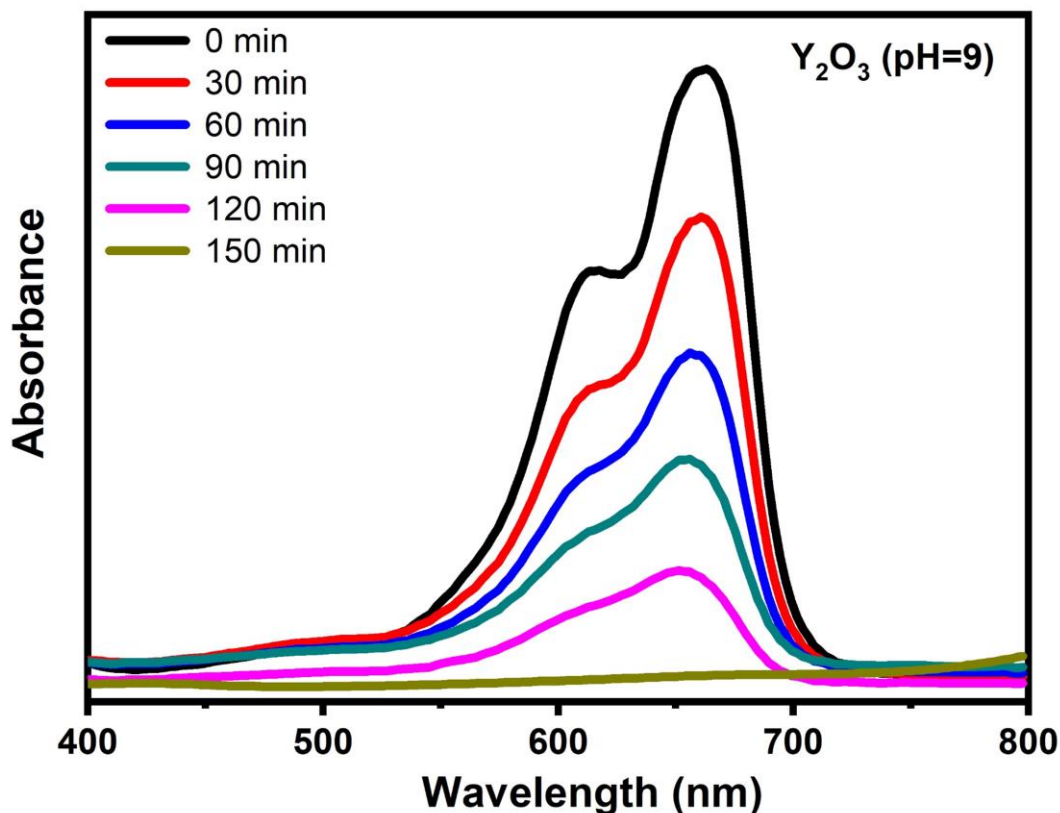


Fig.7 Absorbance spectrum of MB with Y_2O_3 (pH=9) sample under nature solar light irradiation

3.8. Antibacterial activity

The antibacterial studies of Y_2O_3 (pH=9) were assessed adjacent to *Staphylococcus aureus* and *Salmonella typhi* bacterial strains and were checked at diverse concentrations (50 and 100 $\mu\text{g/mL}$). Y_2O_3 nanorods demonstrated good antibacterial action against *Staphylococcus aureus* (20 mm) at 100 $\mu\text{g/mL}$. Table 2 recapitulates the zone of inhibition (ZOI) values acquired adjacent to both tested microbes.

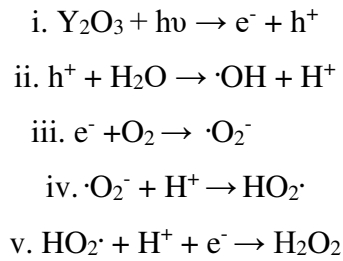
The antibacterial mechanism of the fabricated Y_2O_3 can be elucidated by [35- 37]

- I. Production of reactive oxygen species (ROS)

II. Release of heavy metal ions

The production of ROS on the surface of prepared nanomaterials has accounted by Karthik et al. [38]. Y_2O_3 nanorods have created ROS via the Fenton reaction (FR) directing to lipid peroxidation, injure of DNA, and decay of protein possibly obliterate bacteria without detrimental normal cells. The ROS (from Y_2O_3 nanorods) manipulated the oxidative stress in the intracellular functional alterations (bacteria cell wall connect with the mesosome) and foremost to the cell bereavement.

Typically, the antibacterial action chiefly varies upon the specific surface area, crystallite size, and diverse morphologies. Y_2O_3 nanoparticles provide ROS via the FR as follows:



Maria Magdalane et al. have stated the Y^{3+} from the Y_2O_3 nanoparticles [1]. Based on the Maria Magdalane et al. report, the discharged Y^{3+} from the Y_2O_3 nanorods take action as positive and the cell wall takes action as a negative charge, they are evenly engrossed. Such communication can guide to decay of proteins, failure of DNA reproduction capability, and subsequently, the bereavement of the bacterium [39-41].

Table 2. The ZOI values of the prepared Y_2O_3 (pH=9) by co-precipitation method

Tested microorganisms	Gram-reaction	ZOI (mm)		Positive control (Streptomycin)	Negative control
		50 $\mu\text{g/mL}$	100 $\mu\text{g/mL}$		
<i>S. aureus</i>	+ve	16	20	28	--
<i>S. typhi</i>	-ve	14	18	22	--

4. Conclusion

The yttrium oxide nanomaterials were effectively fabricated by the co-precipitation route and their structural, surface morphology, optical, photocatalytic, and antibacterial properties were deliberated. XRD pattern confirms the cubic structure of Y_2O_3 . The lower pH values give a less crystallite size and lattice constant compared with the higher pH values. The pH value plays an important role in obtaining Y_2O_3 samples with various morphologies. SEM images show the different morphologies like agglomeration of spherical nanoparticles, cube like and nanorods morphology. The Y_2O_3 samples exhibit two emission peaks NBE UV emission and visible region. The PL intensity of these emissions altered with the morphology of Y_2O_3 nanostructure obtained at different pH values. The Y_2O_3 sample synthesized at pH value 9 possess strong blue emission, nanorods like morphology and good crystallinity can be considered as potential luminescent material for optoelectronic application. Y_2O_3 (pH=9) sample illustrated substantial photocatalytic (adjacent to MB) and antibacterial (against foodborne pathogens) activity. Y_2O_3 (pH=9) sample proves to be an appropriate material for wastewater remediation and biomedical applications.

References

1. C. Maria Magdalane, K. Kaviyarasu, J. Judith Vijaya, B. Siddhardha, B. Jeyaraj, Facile synthesis of heterostructured cerium oxide/yttrium oxide nanocomposite in UV light induced photocatalytic degradation and catalytic reduction: Synergistic effect of antimicrobial studies, *J. Photochem. Photobiol B Biol.* 173 (2017) 23-34.
2. A. Mobeen Amanulla, SK. Jasmine Shahina, R. Sundaram, C. Maria Magdalane, K. Kaviyarasu, Douglas Letsholathebe, S.B. Mohamed, J. Kennedy, M. Maaza, Antibacterial, magnetic, optical and humidity sensor studies of β - $CoMoO_4$ - Co_3O_4 nanocomposites and its synthesis and characterization, *J. Photochem. Photobiol B Biol.* 183 (2018) 233-241.
3. C. Maria Magdalane, K. Kaviyarasu, G. Maria Assuntha Priyadharsini, A.K.H. Bashir, N. Mayedwa, N. Matinise, Abdulgalim B. Isaev, Naif Abdullah Al-Dhabi, Mariadhas Valan Arasu, S. Arokiyaraj, J. Kennedy, M. Maaza, Improved photocatalytic decomposition of aqueous Rhodamine-B by solar light illuminated hierarchical yttria nanosphere decorated ceria nanorods, *J. Mater. Res. Technol.* 8 (3) (2019) 2898-2909.

4. C. Maria Magdalane, K. Kaviyarasu, N. Matinise, N. Mayedwa, N. Mongwaketsi, Douglas Letsholathebe, G.T. Mola, Naif AbdullahAl-Dhabi, Mariadhas Valan Arasu, M. Henini, J. Kennedy, M. Maaza, B. Jeyaraj, Evaluation on La₂O₃ garlanded ceria heterostructured binary metal oxide nanoplates for UV/ visible light induced removal of organic dye from urban wastewater, *S. Afr. Chem. Eng.* 26 (2018) 49-60.
5. K. Kaviyarasu, C. Maria Magdalane, D. Jayakumar, Y. Samson, A.K.H. Bashir, M. Maaza, Douglas Letsholathebe, Ahmed Hossam Mahmoud, J. Kennedy, High performance of pyrochlore like Sm₂Ti₂O₇ heterojunction photocatalyst for efficient degradation of Rhodamine-B dye with waste water under visible light irradiation, *J. King Saud. Univ. Sci.* 32 (2) (2020) 1516-1522.
6. S. Panimalar, R. Uthrakumar, E. Tamil Selvi, P. Gomathy, C. Inmozhi, K. Kaviyarasu, J. Kennedy, Studies of MnO₂/g-C₃N₄ hetrostructure efficient of visible light photocatalyst for pollutants degradation by sol-gel technique, *Surf. Interfaces* 20 (2020) 100512.
7. T. Yamaguchi, N. Ikeda, H. Hattori and K. Tanable, Surface and catalytic properties of cerium oxide, *J. Catal.* 67 (1981) 324-330.
8. G. Blasse, B. C. Grabmair, A general introduction to luminescence materials, *Luminescent Materials*, Springer-verlag, Berlin, 1994.
9. C. Feldmann, T. Justel, C. R. Ronda, P. Schmidt, *Inorganic Luminescent Materials: 100 Years of Research and Application*, *J. Adv. Funct. Mater* 13 (2003) 511-516.
10. S. Nie, S. R. Emory, Probing Single Molecules and Single Nanoparticles by Surface-Enhanced Raman Scattering, *Science* 275 (1997) 1102-1106.
11. A. Sathiya Priya, D. Geetha, K. Karthik, M. Rajamoorthy, Investigations on the enhanced photocatalytic activity of (Ag, La) substituted nickel cobaltite spinels, *Solid State Sci.* 98 (2019) 105992.
12. T. Hirai, Y. Asada and I. Komasaawa, Preparation of ZnO nanoparticles in a reverse micellar system and their photoluminescence properties, *J. Colloid Interface Sci.* 284, (2005) 184-189.

13. L. Lin, S.A. Starostin, S. Li, S.A. Khan, V. Hessel, Synthesis of yttrium oxide nanoparticles via a facile microplasma-assisted process, *Chem. Eng. Sci.* 178 (2018) 157-166.
14. O. Singh, M. Palsingh, N. Kohli and R. Chand singh, Effect of pH on the morphology and gas sensing properties of ZnO nanostructures, *Sens. Actuators B Chem.* 166-167 (2012) 438 -443.
15. J. Dhanaraj, R. Jagannathan, T. R.N. Kutty, C. H. Lu, Photoluminescence Characteristics of $Y_2O_3:Eu^{3+}$ Nanophosphors Prepared Using Sol–Gel Thermolysis. *J. Phys.Chem.B* 105 (2001) 11098-11105.
16. H. Tomaszewski, h. Weglarz, R. D. Gryse, Crystallization of yttria under hydrothermal conditions, *J. Eur. Ceram. Soc.*17 (1997) 403-406.
17. T. Ye, Z. Guiwen, Z. Weiping, X. Shangda, Combustion synthesis and photoluminescence of nanocrystalline $Y_2O_3:Eu$ phosphors, *Mater. Res. Bull.*32 (1997) 501-506.
18. A. P. Jadhav, A. Pawar, C. W. kim, H. G. Cha, U. pal, Y. S. Kang, Effect of Different Additives on the Size Control and Emission Properties of $Y_2O_3:Eu^{3+}$ Nanoparticles Prepared through the Coprecipitation Method, *J. Phys. Chem. C*113 (2009) 16652-16657.
19. P. Scherrer, Bestimmung der Grosse und der inneren Struktur von Kolloidteilchen Mittels Rontgenstrahlen, *Nachrichten von der Gesellschaft der Wissenschaften, Gottingen. MathPhys Kl* 2 (1918) 98-100.
20. J. Chen, L. Yaling, Y. Wang, J. Yun, D. Cao, Preparation and characterization of zinc sulfide nanoparticles under high-gravity environment, *Mat. Res. Bull.* 39(2) (2004) 185-194.
21. S. Lakshmanaperumal, P. Hemalatha, M. Alagar, K. N. Pandiyaraj, Investigation of Structural, Optical and Photocatalytic Properties of Sr Doped ZnO Nanoparticles, *Int. J. Chem. Phys. Sci.* 4 (2015) 1-13.

22. P. Hemalatha, S.N. Karthick, K.V. Hemalatha, M. Yi, Hee-Je Kim, M. Alagar, La-doped ZnO nanoflower as photocatalyst for methylene blue dye degradation under UV irradiation. *J. Mater. Sci. Mater. Electron.* 27 (2016) 2367-2378.
23. M. Kottaisamy, D. Jeyakumar, R. Jegnnathan, M. M. Rao, Yttrium oxide: Eu³⁺ red phosphor by self-propagating high temperature synthesis, *Mater.Res. Bull.* 31 (1996) 1013-1020.
24. R. Murugesan, S. Sivakumar, K. Karthik, P. Anandan, M. Haris, Structural, optical and magnetic behaviors of Fe/Mn-doped and co-doped CdS thin films prepared by spray pyrolysis method, *Appl. Phys. A*, 125 (2019) 281.
25. J. I. Pankove, *Optical process in semiconductors*, Prentice- Hall, New Jersey, 1971.
26. J. Kennedy, P.P. Murmu, J. Leveneur, A. Markwitz, J. Futter, Controlling preferred orientation and electrical conductivity of zinc oxide thin films by post growth annealing treatment, *Appl. Surf. Sci.* 367 (2016) 52-58.
27. Prakasit Intaphong, Anukorn Phuruangrat, K. Karthik, Phattranit Dumrongrojthanath, Titi pun Thongtem, Somchai Thongtem, Effect of pH on phase, morphology and photocatalytic properties of BiOBr synthesized by hydrothermal method, *J. Inorg. Organomet. Polym. Mater.* 30 (2020) 714-721.
28. V. Rajendran, K. Anandan, Different ionic surfactants assisted solvothermal synthesis of zero-, three and one-dimensional nickel oxide nanostructures and their optical properties, *Mater. Sci. Semicond. Process.* 38 (2015) 203-208.
29. S. Mohseni Meybodi, S.A. Hosseini, M. Rezaee, S.K. Sadrnezhaad, D. Mohammadyani, Synthesis of wide band gap nanocrystalline NiO powder via a sonochemical method, *Ultrason. Sonochem.* 19 (2012) 841-845.
30. K. Karthik, V. Revathi, Tetiana Tatarchuk Microwave-assisted green synthesis of SnO₂ nanoparticles and their optical and photocatalytic properties, *Mol. Cryst. Liq. Cryst.* 671:1 (2018) 17-23.

31. Parangusan, H., Ponnamma, D., Al-Maadeed, M.A.A. and Marimuthu, A, Nanoflower-like Yttrium-doped ZnO Photocatalyst for the Degradation of Methylene Blue Dye, *Photochem. Photobiol.* 94 (2018) 237-246.
32. Parangusan, H., Ponnamma, D, Al-Maadeed, M.A.A, Effect of cerium doping on the optical and photocatalytic properties of ZnO nanoflowers, *Bull. Mater. Sci.* 42 (2019) 179.
33. N. Benameur, M.A. Chakhom, A. Boukhachem, M.A. Dahamni, M. Ghamnia, N. Hacini, J.-P. Pireaux, L. Houssiau, A. Ziouche, Investigation of some physical properties of pure and Co-doped MoO₃ synthesized on glass substrates by the spray pyrolysis method, *Journal of Electron Spectroscopy and Related Phenomena*, Volume 234, 2019, Pages 71-79.
34. M.A. Chakhom, A. Boukhachem, M. Ghamnia, N. Benameur, N. Mahdhi, K. Raouadi, M. Amlouk, An attempt to study (111) oriented NiO-like TCO thin films in terms of structural, optical properties and photocatalytic activities under strontium doping, *Spectrochimica Acta Part A: Molecular and Biomolecular Spectroscopy*, Volume 205, 2018, Pages 649-660.
35. V. Revathi, K. Karthik, Physico-chemical properties and antibacterial activity of Hexakis (Thiocarbamide) Nickel (II) nitrate single crystal, *Chem. Data. Collections* 21 (2019) 100229.
36. Jolly Bhadra, Hemalatha Parangusan, Anton Popelka, Marian Lehocky, Petr Humpolicek, Noora Al-Thani, Electrospun Polystyrene/PANI-Ag fibers for organic dye removal and antibacterial application, *J. Environ. Chem. Eng.* 8 (3) (2020) 103746.
37. R. Aswini, S. Murugesan and K. Kannan, Bio-engineered TiO₂ nanoparticles using *Ledebouria revoluta* extract: Larvicidal, histopathological, antibacterial and anticancer activity, *Int. J. Environ. Anal. Chem.* (2020) doi:10.1080/03067319.2020.1718668.

38. Karthik Kannan, Devi Radhika, Kishor Kumar Sadasivuni, Kakarla Raghava Reddy, Anjanapura V. Raghu, Nanostructured metal oxides and its hybrids for photocatalytic and biomedical applications, *Adv. Colloid Interface Sci.* 281 (2020) 102178.
39. Karthik Kannan, Dhanuskodi Sivasubramanian, Prabukumar Seetharaman, Sivaramakrishnan Sivaperuaml, Structural and biological properties with enhanced photocatalytic behaviour of CdO-MgO nanocomposite by microwave-assisted method, *Optik* 204 (2020) 164221.
40. K. Karthik, S. Dhanuskodi, C. Gobinath, S. Prabukumar, S. Sivaramakrishnan, Fabrication of MgO nanostructures and its efficient photocatalytic, antibacterial and anticancer performance, *J. Photochem. Photobiol B Biol.* 190 (2019) 8-20.
41. Karthik Kannan, D. Radhika, Maria P. Nikolova, Kishor Kumar Sadasivuni, Namitha R, Structural and functional properties of rare earth-based (NiO-CGO) nanocomposite produced by effective multiple doping approach via co-precipitation, *Mater. Technol.* (2020). DOI: [10.1080/10667857.2020.1755555](https://doi.org/10.1080/10667857.2020.1755555).

Figures

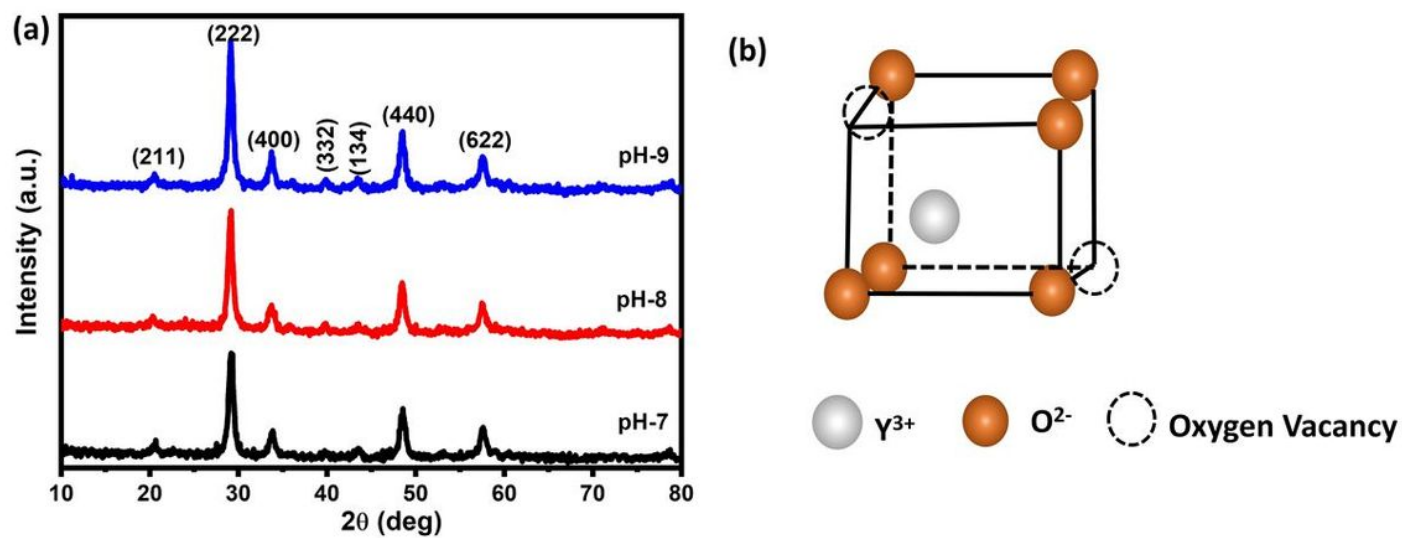


Figure 1

XRD patterns of Y₂O₃ nanoparticles prepared with different pH values

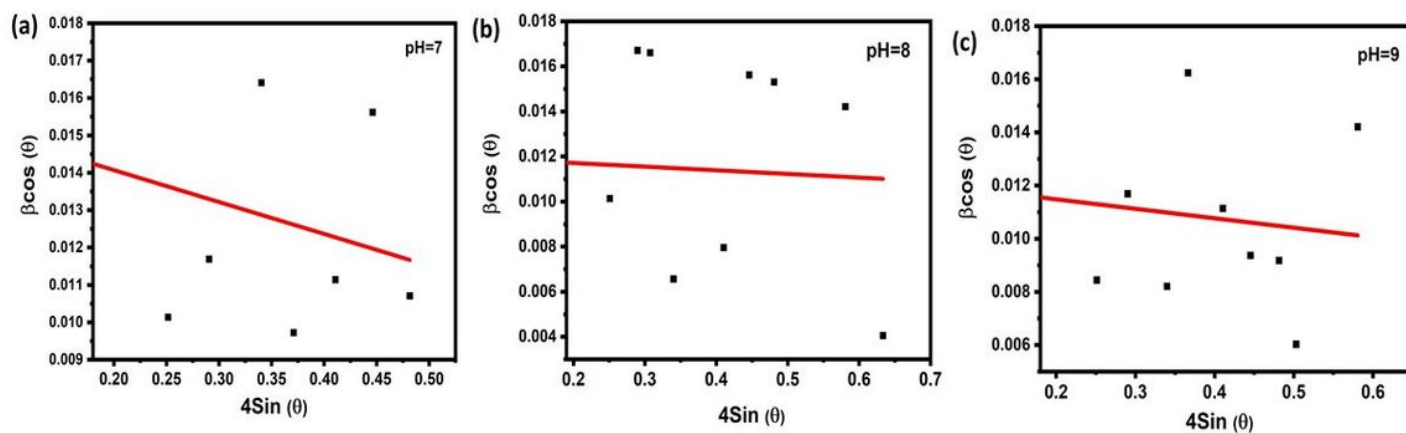


Figure 2

W-H plot for Y₂O₃ nanoparticles synthesized with a different pH value (a) 7 (b) 8 and (c) 9

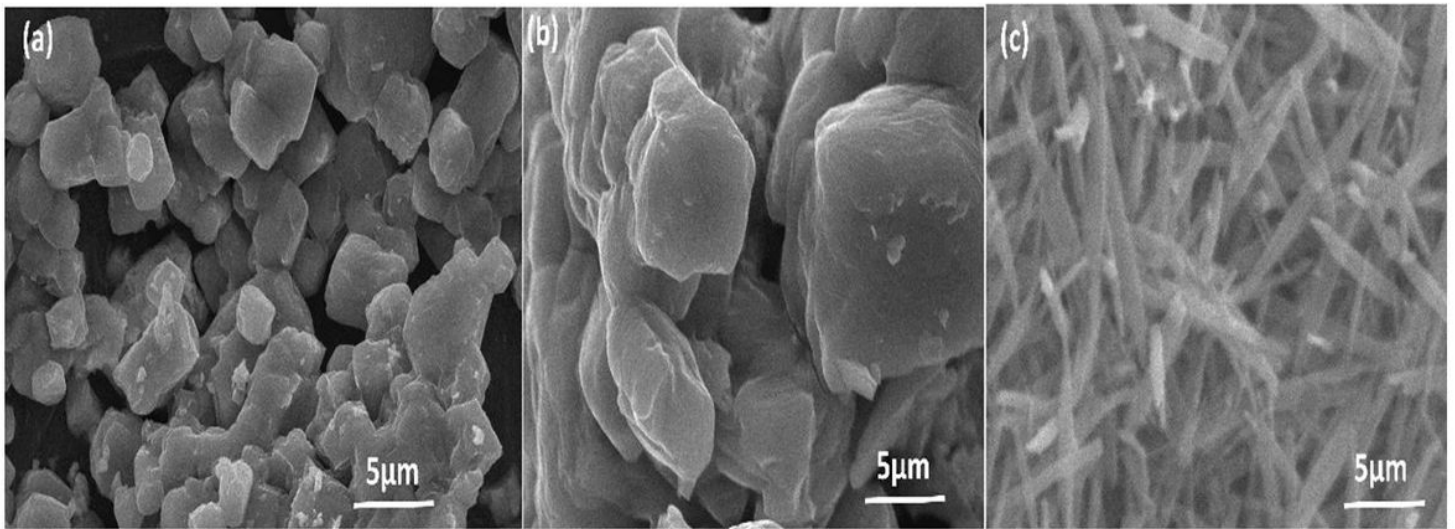


Figure 3

SEM micrographs of Y₂O₃ sample with a diverse pH value (a) pH=7, (b) pH=8 and (c) pH=9

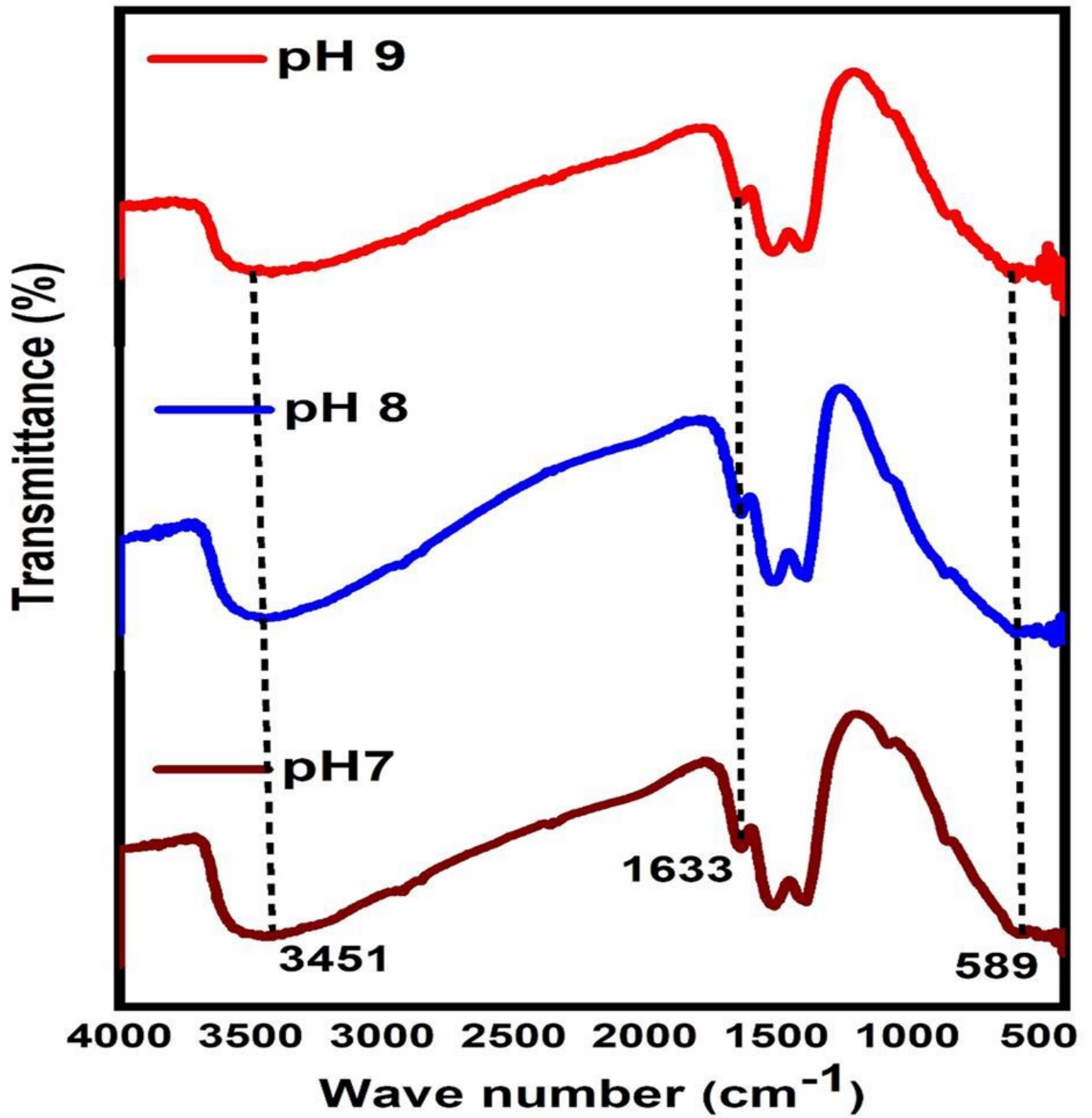


Figure 4

FTIR spectra of Y₂O₃ nanoparticles with a different pH value of 7, 8 and 9

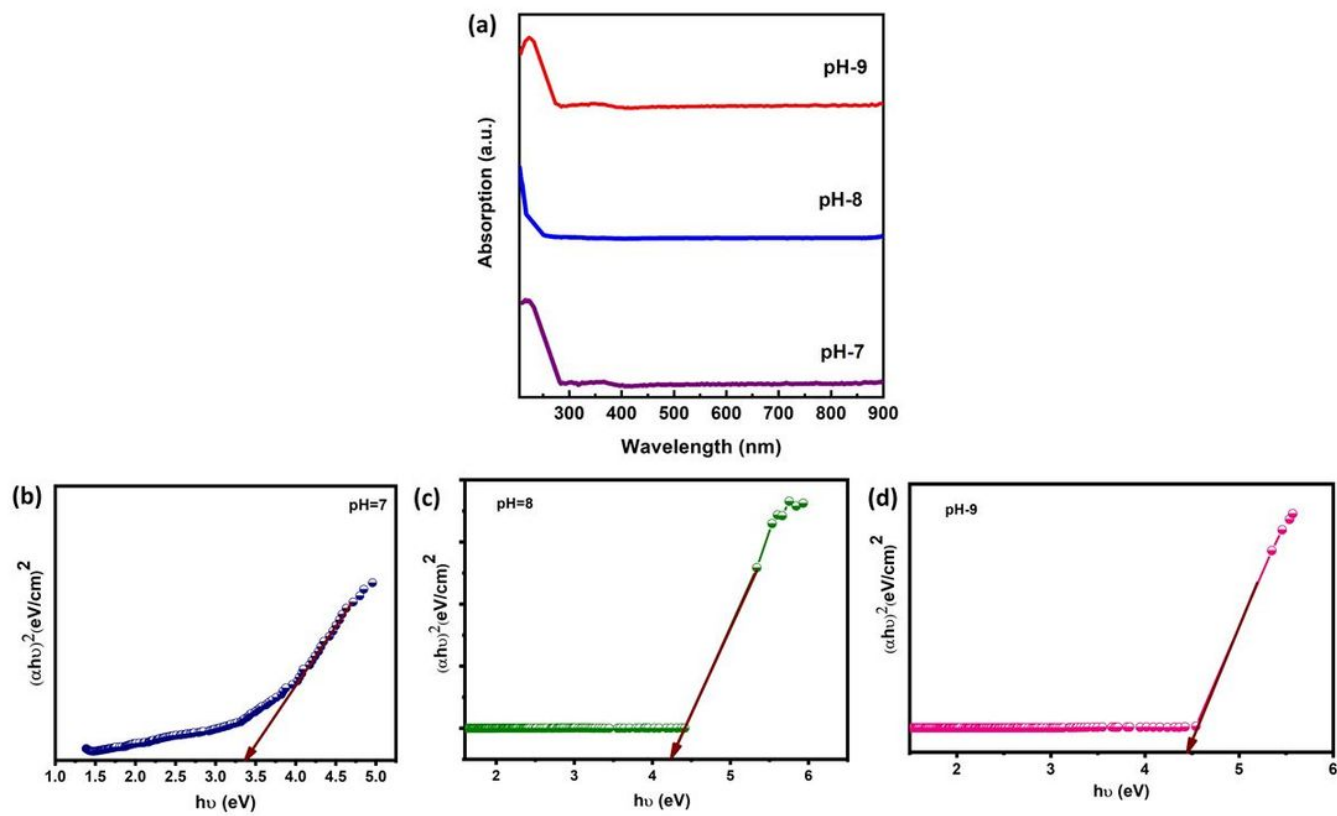


Figure 5

(a) UV-Vis absorption spectra of Y₂O₃ sample and (b-d) bandgap determination of the Y₂O₃ nanoparticles prepared at different pH 7, 8 and 9

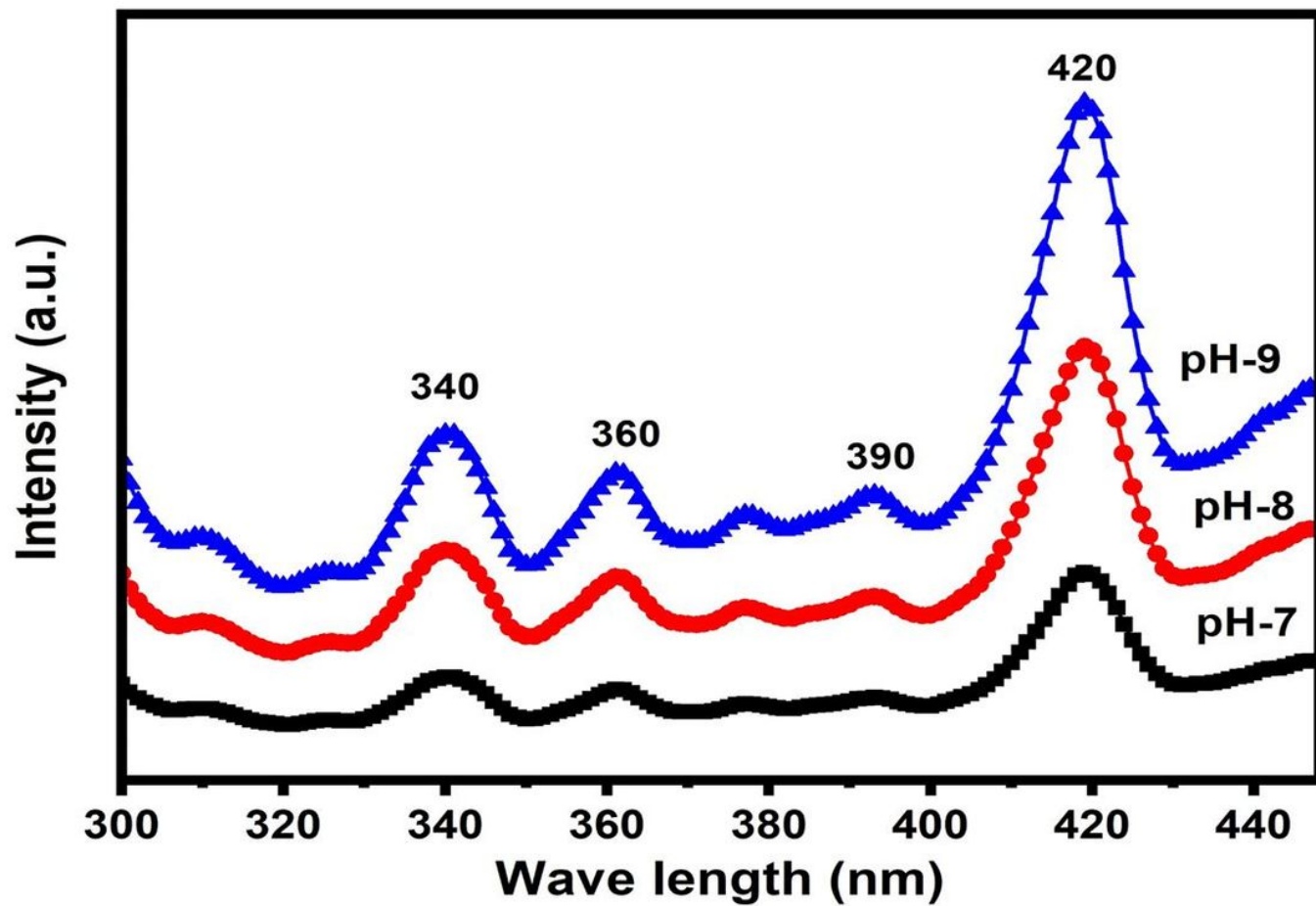


Figure 6

Photoluminescence spectra of Y₂O₃ samples prepared at diverse pH=7, 8 and 9

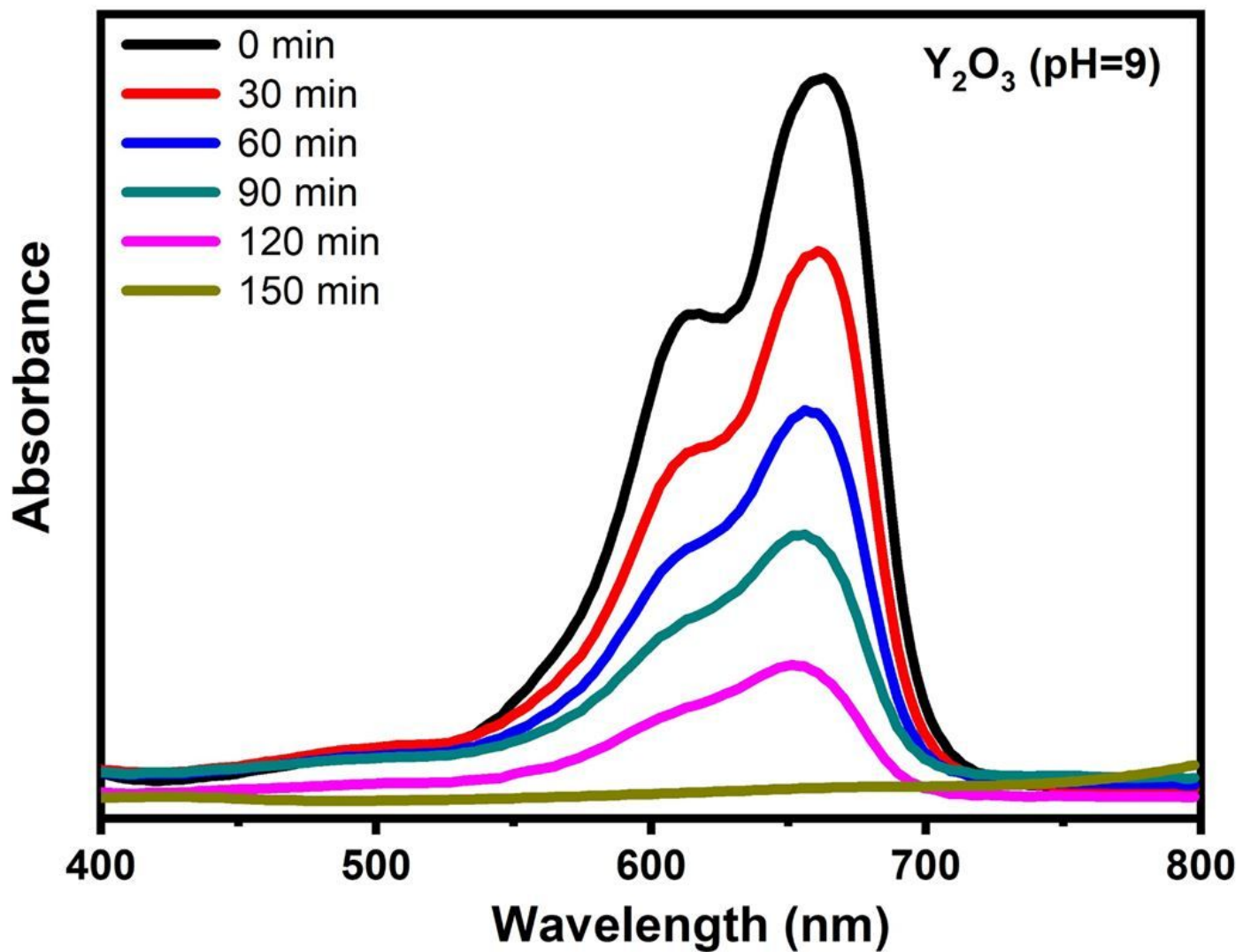


Figure 7

Absorbance spectrum of MB with Y_2O_3 (pH=9) sample under nature solar light irradiation